

This article was downloaded by: [Yale University]

On: 12 May 2011

Access details: Access Details: [subscription number 930573056]

Publisher Taylor & Francis

Informa Ltd Registered in England and Wales Registered Number: 1072954 Registered office: Mortimer House, 37-41 Mortimer Street, London W1T 3JH, UK



Combustion Theory and Modelling

Publication details, including instructions for authors and subscription information:

<http://www.informaworld.com/smpp/title~content=t713665226>

Computational and experimental study of steady axisymmetric non-premixed methane counterflow flames

G. Amantini^a; J. H. Frank^b; M. D. Smooke^a; A. Gomez^a

^a Department of Mechanical Engineering, Yale Center for Combustion Studies, Yale University, New Haven, CT, USA ^b Combustion Research Facility, Sandia National Laboratories, Livermore, CA, USA

To cite this Article Amantini, G. , Frank, J. H. , Smooke, M. D. and Gomez, A.(2007) 'Computational and experimental study of steady axisymmetric non-premixed methane counterflow flames', *Combustion Theory and Modelling*, 11: 1, 47 – 72

To link to this Article: DOI: 10.1080/13647830600792370

URL: <http://dx.doi.org/10.1080/13647830600792370>

PLEASE SCROLL DOWN FOR ARTICLE

Full terms and conditions of use: <http://www.informaworld.com/terms-and-conditions-of-access.pdf>

This article may be used for research, teaching and private study purposes. Any substantial or systematic reproduction, re-distribution, re-selling, loan or sub-licensing, systematic supply or distribution in any form to anyone is expressly forbidden.

The publisher does not give any warranty express or implied or make any representation that the contents will be complete or accurate or up to date. The accuracy of any instructions, formulae and drug doses should be independently verified with primary sources. The publisher shall not be liable for any loss, actions, claims, proceedings, demand or costs or damages whatsoever or howsoever caused arising directly or indirectly in connection with or arising out of the use of this material.

Computational and experimental study of steady axisymmetric non-premixed methane counterflow flames

G. AMANTINI[†], J. H. FRANK[‡], M. D. SMOOKE[†] and A. GOMEZ^{*†}

[†]Department of Mechanical Engineering, Yale Center for Combustion Studies, Yale University, New Haven, CT 06520, USA

[‡]Combustion Research Facility, Sandia National Laboratories, Livermore, CA 94551, USA

(Received 9 November 2005; in final form 8 May 2006)

We investigated computationally and experimentally the structure of steady axisymmetric, laminar methane/enriched-air diffusion flames. Experimentally, we imaged simultaneously single-photon OH LIF and two-photon CO LIF, which also yielded the forward reaction rate (RR) of the reaction $\text{CO} + \text{OH} \rightarrow \text{CO}_2 + \text{H}$. In addition, particle image velocimetry (PIV) was used to measure the velocity in the proximity of the fuel and oxidizer nozzles, providing detailed boundary conditions for the simulations. Computationally, we solved implicitly the steady state equations in a modified vorticity–velocity formulation on a non-staggered, non-uniform grid. We compared the results along the axis of symmetry from the two-dimensional simulations with those from the one-dimensional model, and showed consistency between them. The comparison between the experimental and computational data yielded excellent agreement for all measured quantities. The field of these two-dimensional flames can be roughly partitioned into two regions: the region between the two reactant nozzles, in which viscous and diffusive effects are confined to the mixing layer and to the nozzle walls, where separation occurs; and a radial development region, which is initially confined by recirculation zones near the burner flanges. Buoyancy is virtually irrelevant in the first region at all but the smallest, and practically irrelevant, strain rates. Buoyancy, on the other hand, does play a role in the growth of the recirculation zones, and in determining the flame location in the outermost region.

Keywords: Counterflow; Diffusion; Flames; Vorticity–velocity formulation

Notation

A	global strain rate
$c_{p,k}$	specific heat capacity at constant pressure for the k th species
div	divergence operator
D	Brownian diffusivity
D_T	thermal diffusivity of the mixture
g	gravity acceleration
h_k	total enthalpy for the k th species
HR	global heat release
HR_i	the heat release associated with the i th reaction
$k(T)$	forward rate constant of the elementary reaction $\text{CO} + \text{OH} \rightarrow \text{CO}_2 + \text{H}$
NSPEC	total number of species present in the chemical mechanism

*Corresponding author. E-mail: alessandro.gomez@yale.edu

r	radius
R	nozzle radius
RR	forward reaction rate of the elementary reaction $\text{CO} + \text{OH} \rightarrow \text{CO}_2 + \text{H}$
T	temperature
\vec{v}	velocity vector
v_r	radial velocity
v_z	axial velocity
$V_{k,r}$	diffusion velocity in the radial direction for the k th species
$V_{k,z}$	diffusion velocity in the axial direction for the k th species
V_T	local particle drift velocity
Y_k	mass fraction of the k th species
Z	mixture fraction
α	tangential momentum accommodation coefficient (assumed to be unity)
α_T	dimensionless thermophoretic diffusion factor
λ	thermal conduction coefficient
μ	viscosity of the mixture
ν	momentum diffusivity of the gas mixture
ρ	density of the mixture
ρ_{HOT}	density of the mixture at the location where the temperature is maximum
ρ_{COLD}	density of the mixture at the location where the temperature is minimum
χ	scalar dissipation rate
χ_{st}	scalar dissipation rate at the stoichiometric surface
ω	vorticity
$\dot{\omega}_k$	production rate for the k th species

Superscripts

FUEL	fuel stream at the nozzle mouth
OXID	oxidizer stream at the nozzle mouth
p	particle

1. Introduction

Most of the combustion work on two-dimensional (2D) counterflow flames focuses on the effects of the interaction of counterflow flames with a variety of time-varying perturbations in the vicinity of the axis of symmetry. Katta *et al.* [1] investigated the interaction between different types of perturbations in hydrogen flames, identifying various quenching patterns. In Oh *et al.* [2], the interaction between a single vortex and a methane counterflow flame was simulated. Frouzakis *et al.* [3] simulated 2D hydrogen flames and examined the sensitivity of such flames to the inlet boundary conditions. Lee *et al.* [4] and Frouzakis *et al.* [5] studied the transition from a hydrogen diffusion flame to an edge flame, capturing extinction and reignition phenomena by impulsively perturbing the steady state flame.

The purpose of this contribution is to perform a computational study of axisymmetric methane counterflow flames and to validate it quantitatively with experimental results – a task hitherto unfulfilled in the literature. Although comparisons between 2D computations and experimental results have already been attempted in unsteady counterflow flames [6], they were only qualitative in nature and limited in scope. The interpretation of the experimental results in [6] was further complicated by the multiple length and time scales that

were introduced by injecting vortices of different sizes into the fuel and the oxidizer flows. A broader comparison encompassing multiple variables and, most importantly, velocity fields is essential to validate the computational approach. As Frouzakis *et al.* [3] showed, the sensitivity of counterflow flames to the inlet boundary conditions is significant. Matching the computational and experimental inlet velocity boundary conditions in detail is the only viable way for a 2D code to replicate accurately the experimental data. To date, no such match has been attempted. Furthermore, validation against steady, one-dimensional (1D) experimental data, as in [2] and [7], is a necessary but not sufficient condition to guarantee code reliability.

In this contribution, a steady 2D axisymmetric methane/enriched-air laminar opposed-jet diffusion flame is analysed both computationally and experimentally, as a necessary step towards future modelling of vortex-flame interactions. Experimentally, we imaged simultaneously single-photon OH laser-induced fluorescence (LIF) and two-photon CO LIF, the combination of which also yielded the forward reaction rate (RR) of the reaction $\text{CO} + \text{OH} \rightarrow \text{CO}_2 + \text{H}$. In addition, particle image velocimetry (PIV) was used to measure velocities in the proximity of the fuel and oxidizer nozzles, providing detailed boundary conditions for the computational simulations. Computationally, a modified vorticity–velocity formulation was developed, and it is shown that the formulation described in [8] experiences mass gain or loss depending on the nature of the starting estimate. In order to obtain a mass-conservative solution, the Poisson-like equation for radial velocity was replaced by the continuity equation, and mass conservative solutions that closely match the experimental data were obtained. This modified vorticity–velocity formulation retains two distinct advantages: first, pressure does not explicitly appear in the differential equations, and thus difficulties associated with the determination of the pressure boundary conditions, especially at the outflow boundary, are avoided; second, the boundary conditions for this formulation are clearer and easier to impose than those based on stream function or vector-potential formulations.

2. Experimental methods

2.1 Burner

A schematic diagram of the experimental system, consisting of two lasers, two cameras and an axisymmetric counterflow burner, is shown in figure 1. Each side of the burner was composed of a contoured 12.5 mm diameter nozzle. The nozzles were surrounded by 76.2 mm diameter flanges to provide well-specified boundary conditions. The flanges were water cooled to maintain a constant wall temperature. The bottom portion of the burner was surrounded by a coflowing nitrogen shroud to isolate the flame from external disturbances. The nozzle separation distance was kept constant at 13 mm. The CH_4/N_2 mixture flowed from the top nozzle, and the O_2/N_2 mixture flowed from the bottom nozzle.

2.2 OH LIF, CO LIF and reaction rate imaging

For the OH LIF measurements, the frequency-doubled output from a Nd:YAG-pumped dye laser was tuned near 285 nm to pump the $Q_1(12)$ transition of the A–X(1, 0) band. An intensified CCD camera (512×512 pixels) with an $f/1.8$ Cerco quartz camera lens was used to record the OH LIF signal with a projected pixel size of $93.6 \mu\text{m} \times 93.6 \mu\text{m}$. The image intensifier was gated for 400 ns bracketing the dye laser pulse. The OH LIF images were

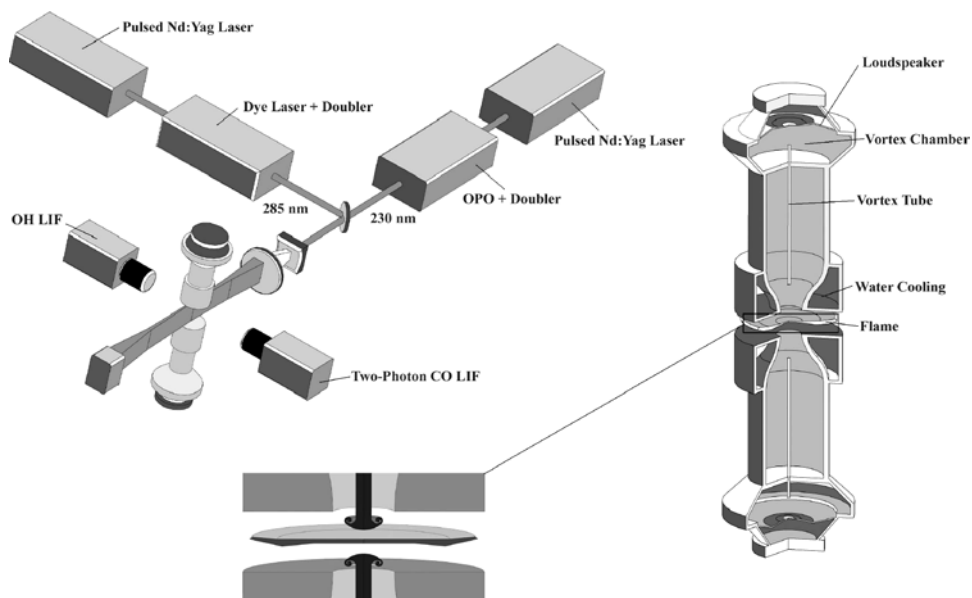


Figure 1. Experimental set-up for simultaneous imaging of OH LIF and two-photon CO LIF. Insets: schematic of the axisymmetric counterflow burner.

corrected for spatial variations in the laser sheet using acetone LIF to record the beam profile. Two-photon CO LIF was excited by pumping overlapped transitions in the B-X(0,0) Hopfield-Birge system of CO using the frequency-doubled output from a Nd:YAG-pumped optical parametric oscillator (OPO) (14 mJ) near 230.1 nm. The laser was tuned to maximize the CO LIF signal in a laminar, non-premixed methane counterflow flame. Sheet forming optics were used to form an 11.5 mm high laser sheet. The average laser beam profile was measured using CO LIF obtained from a mixture of CO in N₂ (0.1% CO by volume). The image intensifier was gated for 600 ns, bracketing the OPO laser pulse. The CO fluorescence was imaged onto an intensified CCD camera (512 × 512 pixels) with a *f*/1.2 camera lens and an interference filter ($\lambda = 484$ nm and $\Delta\lambda = 10$ nm) which transmitted fluorescence from the B–A (0, 1) transition at 483.5 nm and blocked out-of-band interference. The projected pixel size was 93.6 $\mu\text{m} \times 93.6$ μm . Timing of the two laser pulses was controlled with digital delay generators. The OPO laser fired 600 ns after the dye laser to eliminate the possibility of cross-talk between the two diagnostics.

The forward reaction rate of the reaction $\text{CO} + \text{OH} \rightarrow \text{CO}_2 + \text{H}$ was measured by simultaneous imaging of single-photon OH LIF and two-photon CO LIF. This reaction is the dominant pathway for CO₂ production in CH₄/air flames. The reaction rate imaging technique is described in detail elsewhere [9, 10], and only a brief overview is given here. The forward reaction rate, RR, is given by $\text{RR} = k(T)[\text{CO}][\text{OH}]$. The product of the LIF signals from CO and OH can be approximated by $f_{\text{CO}}(T)f_{\text{OH}}(T)[\text{CO}][\text{OH}]$, where the temperature dependence of the LIF signals is represented by $f(T)$. The pump/detection scheme determines the temperature dependence of the LIF signals and can be selected such that $f_{\text{OH}}(T)f_{\text{CO}}(T) \propto k(T)$. When this relationship is achieved, the pixel-by-pixel product of the OH LIF and CO LIF signals is proportional to the reaction rate.

The reaction rate imaging technique requires careful matching of the OH and CO LIF images. A precise image matching technique was used to obtain accurate registration between

the two CCD cameras [9]. Images were matched with an eight parameter bilinear geometric warping algorithm, and the residual matching error was in the subpixel range.

2.3 PIV measurements

Velocity field measurements were performed using PIV. The fuel and oxidizer flows were seeded with oil droplets, that were consumed in the reaction zone. The PIV system (TSI) consisted of two pulsed Nd:YAG lasers and a 2000×2000 pixel charge-coupled device (CCD) camera. The laser beams were formed into overlapping sheets, which intersected the burner axis. The lasers were sequentially pulsed with a $150 \mu\text{s}$ time delay, and the particle scattering from each laser pulse was imaged onto a separate frame of the camera. Velocity vectors were determined using a cross-correlation analysis with 32×32 pixel ($0.675 \text{ mm} \times 0.675 \text{ mm}$) interrogation regions separated by 16 pixels. PIV data were averaged over ten consecutive sets of data, with uncertainties estimated at 3 cm/s.

In section 4, the experimental flow field will be compared with the computational flow field. Two effects are taken into account in the computational velocity fields: first, the vaporization of the oil droplets, and second, thermophoresis. The former effect has been included by masking all the vectors corresponding to a local temperature larger than the boiling point of the oil. Thermophoretic effects were evaluated from the computational velocity field in the particle-laden region according to the relations provided by [11]. The local particle drift velocity was obtained using

$$V_T = (\alpha_T D)_p \cdot (-\nabla T/T) \cong 0.75 \cdot [1 + \pi/8 \cdot \alpha] \cdot v \cdot (-\nabla T/T) \quad (1)$$

These effects are important in the immediate vicinity of the flame where the temperature gradients are steepest. In such regions, the local particle drift velocity becomes larger than the uncertainty in the PIV data, and the thermophoretic effects need to be included in the computational velocity field.

2.4 Inlet experimental velocity boundary conditions

The behaviour of the steady velocity profile at the inlet nozzles was investigated for self-similarity at different strain rates, using PIV data from four different steady flames. The feed compositions of these flames are reported in table 1. The velocity profiles for the four flames are displayed in figures 2(a) and (b) for the top and bottom nozzles, respectively. The velocities on the axis range from 39 to 71 cm/s. In figure 2(c), the velocity profiles for each nozzle are non-dimensionalized with respect to the average velocity and the nozzle radius. The resulting eight non-dimensional velocity profiles (two velocity profiles per flame) exhibit excellent self-similarity. The curve in figure 2(c) is a least squares fit to the dimensionless profiles using an eighth degree polynomial whose coefficients were determined using Mathematica [12]. The

Table 1. Compositions (mole fractions) of the fuel and oxidizer streams for flames 1, 2, 3, 4.

Flame	Methane (diluted in N ₂) mole fraction	Oxygen (diluted in N ₂) mole fraction
1	0.225 (top nozzle)	0.367 (bottom nozzle)
2	0.213 (top nozzle)	0.368 (bottom nozzle)
3	0.209 (top nozzle)	0.368 (bottom nozzle)
4	0.170 (bottom nozzle)	0.367 (top nozzle)

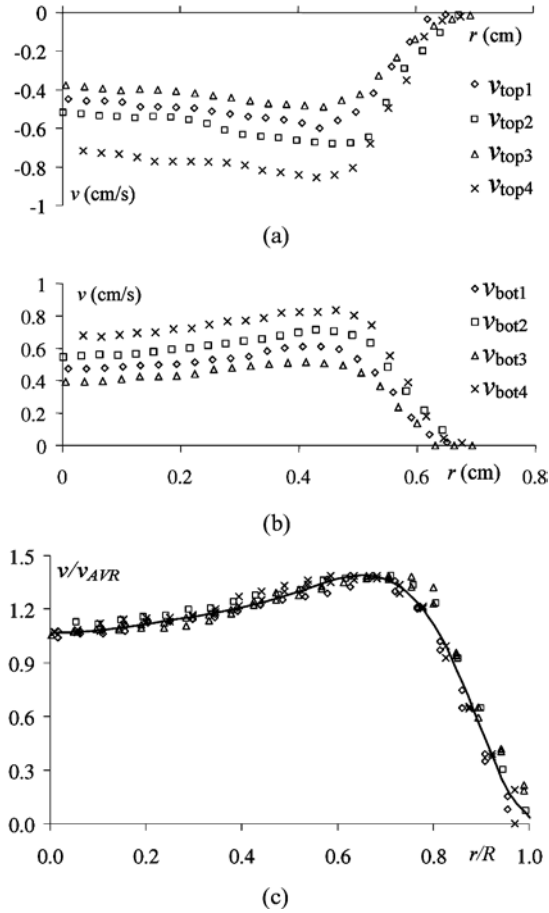


Figure 2. Velocity profiles at the top (a) and bottom nozzles (b) for each of the four flames described in table 1. The non-dimensional velocity profiles, and interpolating polynomial are found in (c).

analytical form of this polynomial is reported below.

$$\frac{v_z(r/R)}{v_{AVG}} = 1.068 + 1.458 \cdot \left(\frac{r}{R}\right)^2 - 7.809 \cdot \left(\frac{r}{R}\right)^4 + 36.99 \cdot \left(\frac{r}{R}\right)^6 - 74.35 \cdot \left(\frac{r}{R}\right)^8 + 55.88 \cdot \left(\frac{r}{R}\right)^{10} - 13.20 \cdot \left(\frac{r}{R}\right)^{12}, \quad (2)$$

The reported PIV measurements show that the axial component of the velocity vector at each nozzle exit is relatively uniform in the vicinity of the axis of symmetry and overshoots close to the nozzle wall. When velocity measurements are performed on a single nozzle in a free jet configuration, no overshoot is detected, suggesting that the finite separation between the burners is responsible for this change in the inlet velocity profile. This finding can be explained qualitatively from Bernoulli's principle. On the axis of symmetry at the stagnation plane, the axial velocity is zero and the static pressure is at a maximum. As a result, the streamlines in the proximity of the axis are subject to a larger adverse pressure gradient as compared to those near the nozzle walls, and the overshoot ensues. Notice that despite this inevitable effect, the plug flow assumption still meets the requirements needed for quantitative 1D modelling since the flow is uniform in the vicinity of the centreline. However, the velocity has to be increased by 6.8

percent with respect to the mass averaged value, to account for the radial non-uniformity. In the 2D case, if quantitative comparisons between computational and experimental results are to be obtained, velocity measurements of the inlet boundary conditions are clearly indispensable.

3. Computational methods

3.1 Problem formulation

The computational study examines a steady laminar, counterflowing diffusion flame using an axisymmetric model that employs the gas-phase conservation equations cast in the vorticity–velocity formulation. The result is a strongly coupled, highly nonlinear set of NSPEC+4 elliptic partial differential equations, where NSPEC is the number of gas-phase species. The present study uses a C2 mechanism with 35 species and 173 reactions [13], and the effect of gas phase radiation in the optically thin limit is considered by including a radiation submodel in which H₂O, CO and CO₂ are the significant radiating species [14]. Numerical simulations have been performed with two different sets of partial differential equations. The first set is expressed in terms of two Poisson-like equations for the velocity components together with vorticity transport, energy conservation and species equations. However, this system of equations, once discretized, does not guarantee mass conservation. To ensure that this fundamental requirement is satisfied, one of the velocity equations is removed from the system and is replaced with the continuity equation. The original vorticity–velocity formulation has been discussed previously [8], and we will just restate the equations for the steady laminar flow.

3.2 Governing equations

Listed below in equations (3) to (7) are the governing equations for the radial velocity, the axial velocity, the vorticity, whose only non-zero component is in the azimuthal direction, energy and species, respectively:

$$\frac{\partial^2 v_r}{\partial r^2} + \frac{\partial^2 v_r}{\partial z^2} = \frac{\partial \omega}{\partial z} - \frac{1}{r} \frac{\partial v_r}{\partial r} + \frac{v_r}{r^2} - \frac{\partial}{\partial r} \left(\frac{\vec{v} \cdot \nabla \rho}{\rho} \right) \quad (3)$$

$$\frac{\partial^2 v_z}{\partial r^2} + \frac{\partial^2 v_z}{\partial z^2} = -\frac{\partial \omega}{\partial r} - \frac{1}{r} \frac{\partial v_r}{\partial z} - \frac{\partial}{\partial z} \left(\frac{\vec{v} \cdot \nabla \rho}{\rho} \right) \quad (4)$$

$$\begin{aligned} \frac{\partial^2 \mu \omega}{\partial r^2} + \frac{\partial^2 \mu \omega}{\partial z^2} + \frac{\partial}{\partial r} \left(\frac{\mu \omega}{r} \right) &= \rho v_r \frac{\partial \omega}{\partial r} + \rho v_z \frac{\partial \omega}{\partial z} - \rho \omega \frac{v_r}{r} + \bar{\nabla} \rho \cdot \nabla \frac{\|\vec{v}\|^2}{2} - \bar{\nabla} \rho \cdot g \\ &+ 2 \left(\bar{\nabla}(\text{div}(v)) \cdot \nabla \mu - \nabla v_r \cdot \bar{\nabla} \frac{\partial \mu}{\partial r} - \nabla v_z \cdot \bar{\nabla} \frac{\partial \mu}{\partial z} \right) \quad (5) \end{aligned}$$

$$\begin{aligned} \rho c_p v_r \frac{\partial T}{\partial r} + \rho c_p v_z \frac{\partial T}{\partial z} &= \frac{1}{r} \frac{\partial}{\partial r} \left(r \lambda \frac{\partial T}{\partial r} \right) + \frac{\partial}{\partial z} \left(\lambda \frac{\partial T}{\partial z} \right) - \sum_{k=1}^{\text{NSPEC}} \\ &\times \left[\rho c_{p,k} Y_k \left(V_{k,r} \frac{\partial T}{\partial r} + V_{k,z} \frac{\partial T}{\partial z} \right) \right] - \sum_{k=1}^{\text{NSPEC}} h_k W_k \dot{\omega}_k \quad (6) \end{aligned}$$

$$\rho v_r \frac{\partial Y_k}{\partial r} + \rho v_z \frac{\partial Y_k}{\partial z} = -\frac{1}{r} \frac{\partial}{\partial r} (r \rho Y_k V_{k,r}) - \frac{\partial}{\partial z} (\rho Y_k V_{k,z}) + W_k \dot{\omega}_k \quad (7)$$

where $\bar{\nabla} = (\partial/\partial z, -\partial/\partial r)$ in equation (5). In order to conserve mass, we replace the radial velocity equation in the governing equations with the continuity equation

$$\frac{\partial(\rho v_r)}{\partial r} + \rho \frac{v_r}{r} + \frac{\partial(\rho v_z)}{\partial z} = 0 \quad (8)$$

In the upcoming sections, we will present computational simulations of a flat diffusion flame at steady state, employing both vorticity–velocity formulations. For the sake of brevity, we will call formulation (a) the set of equations (4) to (8), and we will call formulation (b) the set of equations (3) to (7).

3.3 Boundary conditions

PIV measurements are used to specify the inlet velocity boundary conditions at the nozzles. Stray light effects at the solid boundary caused a lack of PIV data in the region 1.1 mm downstream of the nozzle mouths. Hence, the velocity vectors at the burner inlets are extrapolated from the PIV data in the vicinity of the nozzles, and the interpolating polynomial reported in equation (2) is used to describe the general shape of the velocity profile at the nozzle mouth as a function of the nozzle radius and average velocity. No-slip boundary conditions are imposed at the walls, and the temperature is held constant at the value of the water-cooled flanges. On the outflow boundary, all normal derivatives are set to zero. The full set of boundary conditions employed in the computational simulations is reported below.

At the top burner mouth ($r < 0.65$ cm, $z = 1.3$ cm):

$$v_r = 0 \text{ cm/s} \quad v_z = v_z(r/R), \quad v_{AVG} = -46.4 \text{ cm/s} \quad \omega = \frac{\partial v_r}{\partial z} - \frac{\partial v_z}{\partial r}$$

$$T = 353 \text{ K} \quad Y_{\text{CH}_4} = 0.14, \quad Y_{\text{N}_2} = 0.86.$$

At the bottom burner mouth ($r < 0.65$ cm, $z = 0.0$ cm):

$$v_r = 0 \text{ cm/s} \quad v_z = v_z(r/R), \quad v_{AVG} = 46.1 \text{ cm/s} \quad \omega = \frac{\partial v_r}{\partial z} - \frac{\partial v_z}{\partial r}$$

$$T = 323 \text{ K} \quad Y_{\text{O}_2} = 0.4, \quad Y_{\text{N}_2} = 0.6.$$

At the outlet of the computational domain ($r = 4.0$ cm, $0.0 \text{ cm} < z < 1.3$ cm):

$$\frac{\partial(\rho v_r)}{\partial r} + \rho \frac{v_r}{r} + \frac{\partial(\rho v_z)}{\partial z} = 0 \quad \frac{\partial v_z}{\partial r} = 0 \quad \omega = \frac{\partial v_r}{\partial z} - \frac{\partial v_z}{\partial r} \frac{\partial T}{\partial r} = 0 \quad \frac{\partial Y_i}{\partial r} = 0.$$

At the water-cooled flanges ($0.65 \text{ cm} < r < 4.0$ cm, $z = 0.0, 1.3$ cm):

$$v_r = 0 \quad v_z = 0 \quad \omega = \frac{\partial v_r}{\partial z} - \frac{\partial v_z}{\partial r} \quad T = 323 \text{ K} \quad \frac{\partial Y_i}{\partial z} = 0.$$

On the axis of symmetry ($r = 0.0$ cm, $0.0 \text{ cm} < z < 1.3$ cm):

$$v_r = 0 \quad \frac{\partial v_z}{\partial r} = 0 \quad \omega = 0 \quad \frac{\partial T}{\partial r} = 0 \quad \frac{\partial Y_i}{\partial r} = 0.$$

3.4 Flamesheet

To achieve starting solutions for the complex chemistry steady laminar, counterflowing diffusion flames, we used a flamesheet approach based on conservation equations (4), (5) and (8)

and the mixture fraction conservation equation reported below:

$$\frac{1}{r} \frac{\partial}{\partial r} \left(r \rho D_T \frac{\partial Z}{\partial r} \right) + \frac{\partial}{\partial z} \left(\rho D_T \frac{\partial Z}{\partial z} \right) = \rho v_r \frac{\partial Z}{\partial r} + v_z \frac{\partial Z}{\partial z} \quad (9)$$

The original vorticity–velocity formulation uses equations (3), (4), (5) and (9) and is reported in [15]. In this approach, the density is related to the temperature and the pressure by the gas law, and the thermal diffusivity coefficient in the mixture fraction equation is a function of temperature as well.

3.5 Numerical solution

The solution of the governing equations proceeds with an adaptive, nonlinear boundary value method on a 2D computational mesh. The details of this method have been presented elsewhere [8], and only the essential features are outlined here. The governing equations and boundary conditions are discretized using a finite difference technique on a nine-point stencil, transforming the set of partial differential equations into a set of NSPEC+4 strongly coupled, highly non-linear difference equations at each grid point. The resulting system of equations, written in residual form, is solved with a modified Newton’s method in which the Jacobian matrix is periodically re-evaluated. A preconditioned (block Gauss-Seidel) Bi-CGSTAB method solves the linear system within each Newton iteration. Pseudo-transient continuation is employed to ease the convergence of an arbitrary starting estimate on an initial grid. The final computational mesh is adaptively determined through the equidistribution of solution gradient and curvature between adjacent mesh cells. Local properties are evaluated with vectorized and highly optimized transport and chemistry libraries.

4. Results and discussion

4.1 Comparison between the two vorticity–velocity formulations

In this section, we present computational simulations of a flat diffusion flame at steady state, employing both of the vorticity–velocity formulations [formulation (a) and formulation (b)] presented in section 3.2. To check for mass conservation, we shall consider a pill-box control volume of radius r , with top and bottom at the burner inlets. Under steady state conditions, the total inflow at the burner inlets must match the total outflow in the radial direction. Thus

$$-\int_{A_{\text{in}}(r)} \rho |v_z| dA + \int_{A_{\text{out}}(r)} \rho v_r dA = 0 \quad (10)$$

Figure 3 presents the evaluation of mass inflow and outflow, both normalized with the total mass flow rate injected into the burner, as a function of the radial coordinate for the two formulations, for flame 1 reported in table 1. Inflow and outflow agree for the modified vorticity–velocity formulation (a). The original formulation (b), however, exhibits up to a 74% mass gain at the domain outlet. Figures 4(a) and 4(b) show 2D images of temperature contours for formulations (a) and (b), respectively. The radial extension of the flame in formulation (b) is much larger than that of formulation (a), as a result of the artificial mass generation. In general the non-conservative formulation exhibits mass loss or gain depending on the nature of the starting estimate. If, for example, a high strain flame is used as a starting estimate for a low strain flame, mass will be gained.

To validate the mass-conservative vorticity–velocity formulation, the code is compared with 1D results from the counterflow code developed by Chelliah *et al.* [16]. The chemical kinetics and transport properties in both computations are identical. Identical boundary conditions

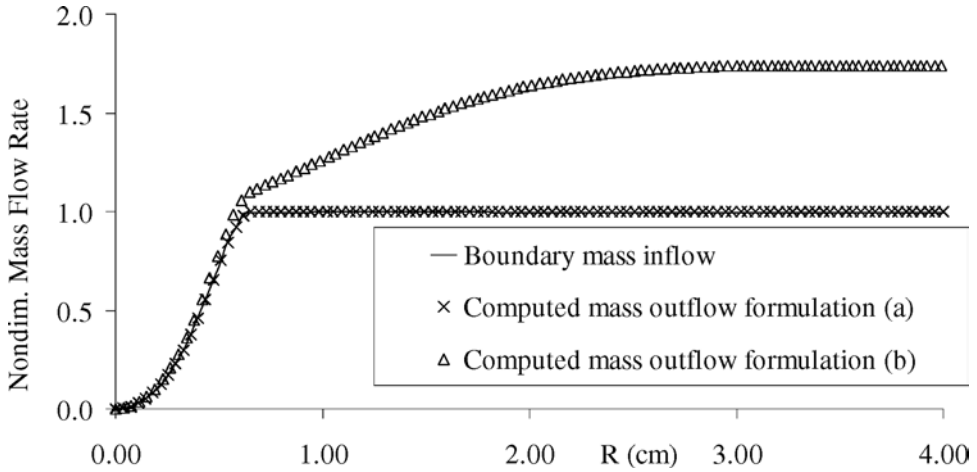


Figure 3. Evaluation of the normalized mass inflow (from boundary conditions) and outflow (from computational data) for formulations (a) and (b).

have been used for both simulations, and $\partial v_z / \partial z$ at the nozzles in the 1D simulation has been computed from the 2D simulation.

Figure 5 illustrates the temperature and axial velocity profiles along the axis of symmetry for the three simulations: the modified vorticity–velocity, the original vorticity–velocity and the 1D

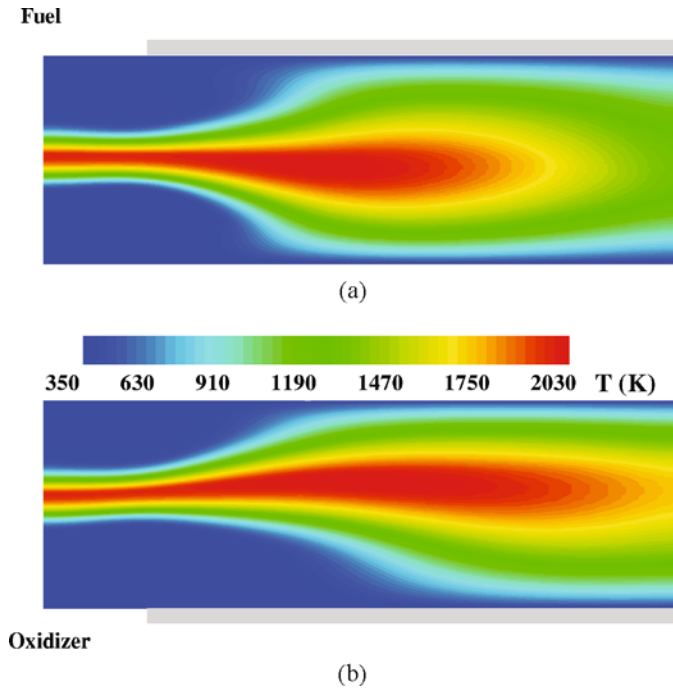


Figure 4. Temperature profiles for the mass-conservative (a) and the non-conservative (b) vorticity–velocity formulations.

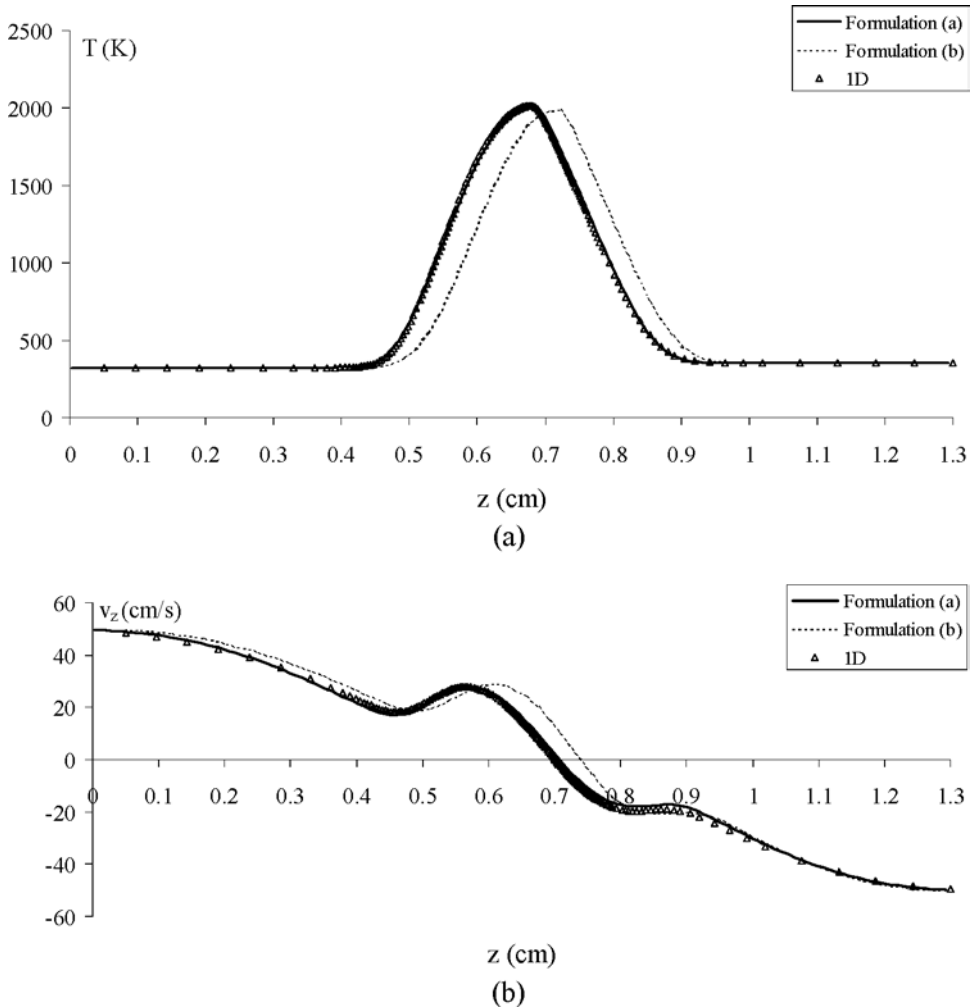


Figure 5. Comparison between 1D and 2D computational results for (a) temperature and (b) axial velocity profiles along the axis of symmetry.

formulation. The modified vorticity–velocity formulation results in excellent agreement with the 1D formulation both for the temperature profile and the centreline axial velocity profile. The original vorticity–velocity model produces computational results that are shifted with respect to the 1D results. In the outer region the flame is not only shifted, but is also qualitatively different in shape from the flame in formulation (a). In view of the results presented in figures 3 to 5, the modified formulation (a) will be used for the remainder of the computational results.

4.2 Comparison between 2D computational and experimental results

We now present comparisons between experimental and computational results for velocity profiles, CO LIF, OH LIF and RR. Figure 6 shows the computational (left) and experimental (right) velocity vectors superimposed on the corresponding axial velocity contours. Both experimental and numerical results are reported with the same scale. The radial and the axial

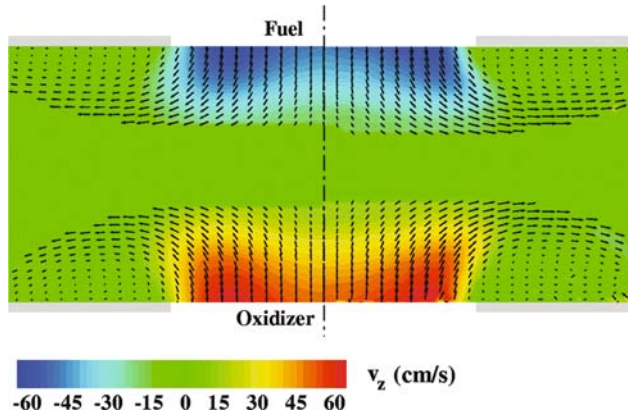


Figure 6. Computational (left) and experimental (right) velocity vectors superimposed onto the axial velocity contours. The radial and the axial dimensions of the images are 1.3 cm and 1.1 cm, respectively.

dimensions of the images are 1.3 cm and 1.1 cm, respectively. In both the computational and the experimental images, there are no vectors in the high-temperature region, since the oil droplets vaporize at approximately 570 K. The computational data are corrected for thermophoretic effects and take into account the vaporization of the oil particles at 570 K. Clearly, the agreement is quantitative, as is further substantiated by an axial scan along the centreline shown in figure 7.

The determination of OH and CO mole fractions from the LIF signals requires additional measurements that are not available in the present study. To facilitate the comparison between the measured LIF signals and the computations, we used the computed species concentrations and temperature to produce simulated LIF signals. These simulated LIF signals can be directly compared with the measurements. To simulate the LIF signals, we computed the collisional quenching rates and Boltzmann fraction populations at each location in the computational domain. The temperature and species-dependent quenching cross-sections for the CO LIF simulations are from [17]. Figures 8(a) and (b) present computational and experimental results for the CO LIF (half domain, 3.2 cm \times 1.1 cm). Both the computational and the experimental

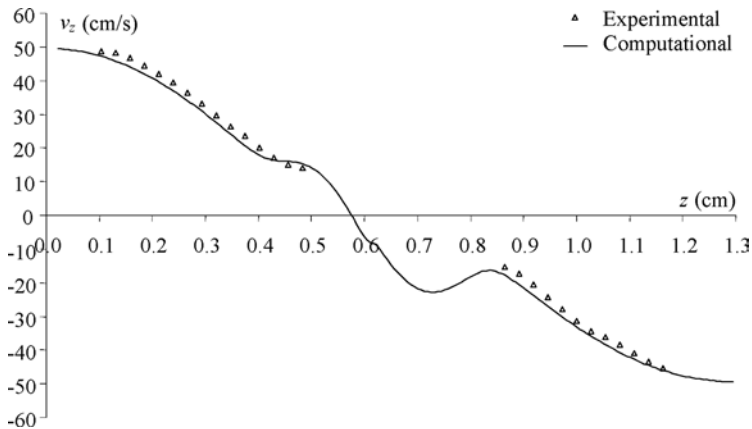


Figure 7. Computational (solid line) and experimental (triangles) centreline axial velocity. The experimental data are reported between $z = 0.1$ cm and $z = 1.2$ cm, consistently with figure 6.

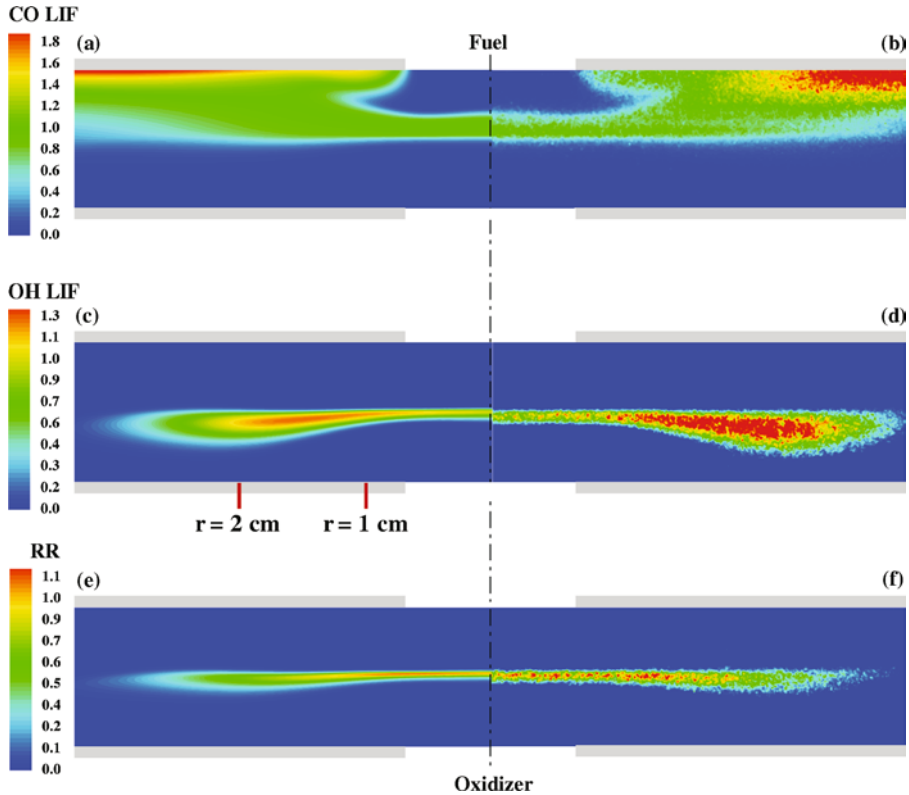


Figure 8. Computational (a) and experimental (b) normalized CO LIF signals, computational (c) and experimental (d) normalized OH LIF signals, and computational (e) and experimental (f) normalized reaction rates. Computational and experimental domains extend 3.2 cm in the radial direction and 1.1 cm in the axial direction.

CO LIF signals have been normalized with respect to the maximum signals obtained along the axis of symmetry. The CO layer at first thins slightly as the radial distance increases, then progressively thickens. The initial thinning of the layer is explained by the higher transverse velocity in the proximity of the nozzle walls. Outside the nozzle region, both components of the velocity vector decrease and the local strain rate reduction accounts for the progressive thickening of the CO layer. The CO build-up in the vicinity of the top flange is a consequence of the recirculation region anchored at the exit of the top nozzle, which leads to entrainment of the long-lived CO produced in the hot region. The agreement between the computational and the experimental results for the CO LIF layer is quantitative everywhere.

Similarly quantitative agreement is shown in the comparison of OH LIF signals [figures 8(c) and (d)] and the reaction rates [figures 8(e) and (f)]. Both the computed and the measured OH LIF signals and RR have been normalized by their respective maxima on the axis of symmetry. The measured OH LIF signal was corrected for background and beam-profile variations. The simulated OH LIF signal was obtained by using the quenching cross-sections for the major OH quenchers given in [18], and the simulated signal includes effects of absorption and beam steering, which are present in the experimental results. The laser beam propagated from the right side of the experimental image towards the left, and consequently the laser energy progressively decreased toward the left side. Laser-beam absorption was incorporated into the simulations by computing the absorbance of OH at each location in the computational domain and determining the cumulative attenuation from the edge of the domain. The OH absorption

cross-sections were estimated from simulations of the OH absorption spectra for temperatures ranging from 800 K to 2300 K using spectroscopic data from reference [19]. The absorption of the laser beam reached a maximum value along the axis of symmetry where the intensity was attenuated to 72% of the value at the edge of the burner. The simulations only included OH absorption since it was the dominant absorbing species. We estimated that CO absorbed only 4% of the laser energy over the region shown in figure 8 using a model for the CO absorption spectrum from reference [20].

Beam steering from index-of-refraction gradients is another effect that must be considered when comparing computed and measured LIF signals in the counterflow geometry. The hot flame layer sandwiched between two layers of low-temperature gases issuing from the nozzles acted as a negative lens spreading the laser beam toward the burner surfaces. Beam steering was incorporated into the simulated OH LIF signal using the algorithm proposed in [20], and the index of refraction of the mixture was computed from the data reported in [22]. Beam steering plays an important role in the proximity of the flanges, but it does not significantly modify the laser intensity field in the hot region. The agreement between the morphology of the computed OH LIF layer and that of the experimental one is good both in the nozzle region and in the outermost region.

More detailed comparisons of the computational and experimental results are illustrated in figures 9 to 11. The figures show normalized plots of measured and calculated CO LIF signal, OH LIF signal and reaction rate as a function of the axial coordinate, z , at three radial positions, $r = 0$ cm, $r = 1$ cm and $r = 2$ cm. Generally, the experimental OH profile and RR profile are broader than the corresponding numerical ones.

4.3 Flame structure

In addition to the radial non-uniformity of the velocity profile that was discussed in connection with figure 2, there is another inherently 2D effect that characterizes the counterflow configuration: the existence of recirculation zones near the nozzle mouths, as a consequence of the sharp corners at the burner inlets, which induce flow separation at all but the lowest strain rates. As will be shown below, the evolution of these recirculation zones depends on the momentum ratio of the two jets, the position of the flame with respect to the stagnation plane, and the global strain rate. In our experiments, we chose the ratio between the momentum of the oxidizer jet and the fuel jet such that the position of the CH* layer would be approximately equidistant from the two nozzles. This resulting momentum ratio was estimated to be 1.4.

Figures 12(a)–(d) present the streamlines superimposed on temperature maps for flames of identical composition and momentum ratio as flame 1, but increasing rate of strain. The global strain rate, A , is defined as [23]:

$$A = \frac{2v_{\text{OXID}}}{L} \left[1 + \frac{v_{\text{FUEL}}}{v_{\text{OXID}}} \cdot \left(\frac{\rho_{\text{FUEL}}}{\rho_{\text{OXID}}} \right)^{\frac{1}{2}} \right] \quad (11)$$

Figure 12(a) shows results from a flame with a strain rate of 26 s^{-1} . A small recirculation zone is located at the exit of the top nozzle, and there is no recirculation zone near the bottom nozzle. While the stagnation plane is approximately equidistant from the top and bottom burners, the thermal layer is shifted to the oxidizer side of the flame. As the strain rate increases, from 77 s^{-1} to 179 s^{-1} [figures 12(b)–(d)], the temperature map becomes more symmetrical, and a recirculation zone appears also near the bottom nozzle. The different recirculation behaviour in the four images can be attributed to two factors: the momentum ratio between the fuel and oxidizer streams and the location of the thermal layer with respect to the stagnation plane. At low strain rates, the temperature layer is thicker and closer to the oxidizer side. As a

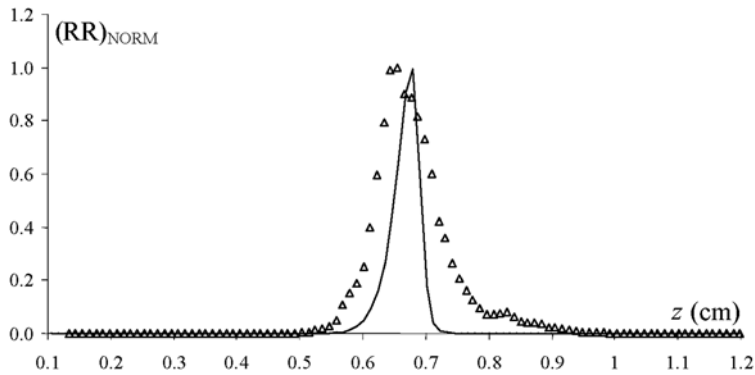
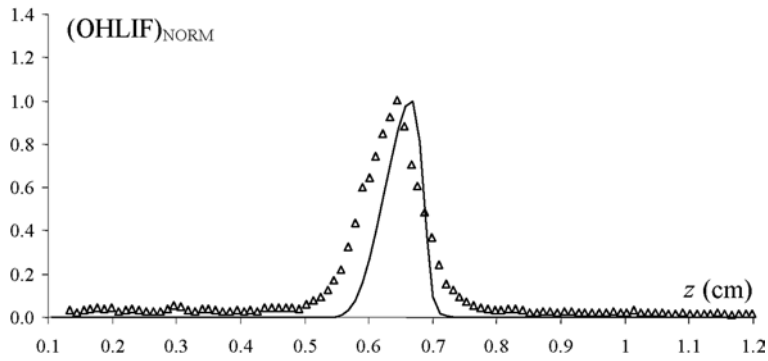
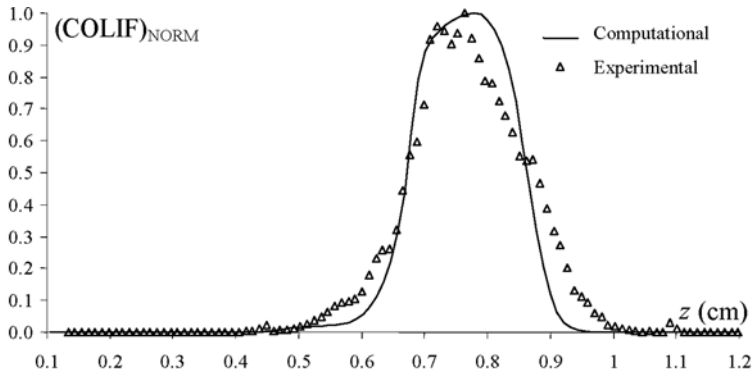


Figure 9. Experimental (triangles) and computational (solid line) normalized CO LIF signals, normalized OH LIF signals, and RR along the axis of symmetry. The oxidizer nozzle is at $z = 0.0$ cm and the fuel nozzle is at $z = 1.3$ cm.

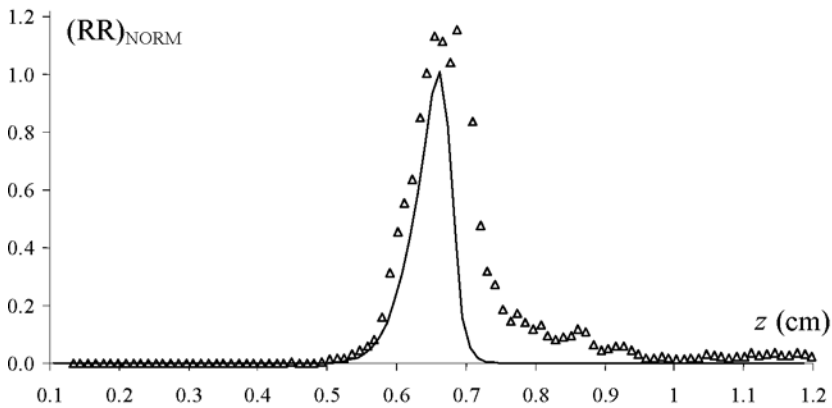
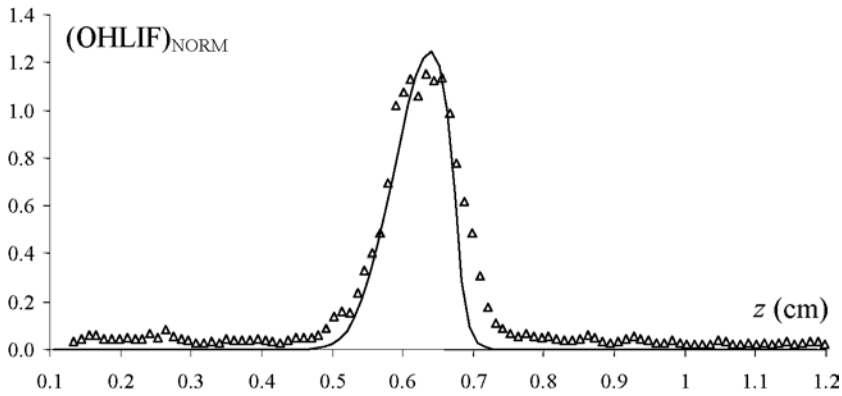
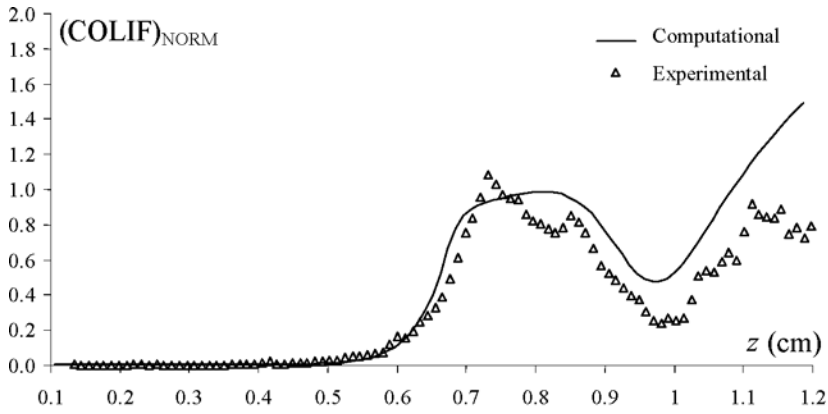
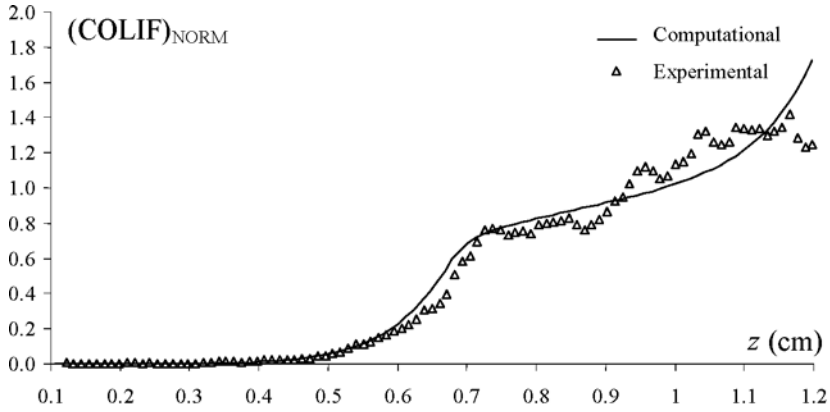
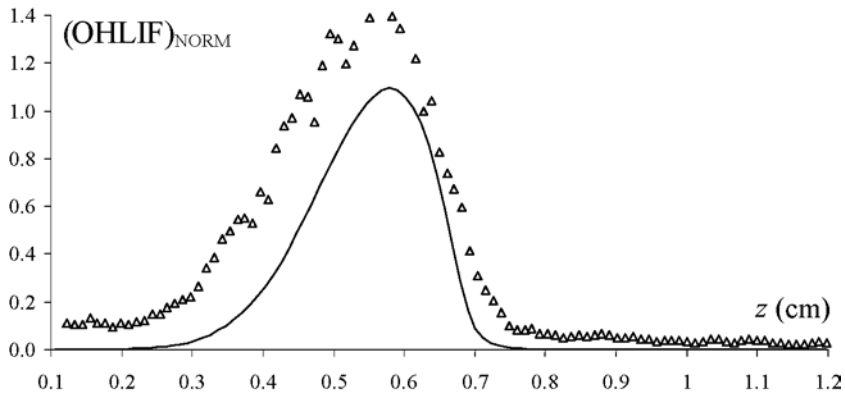


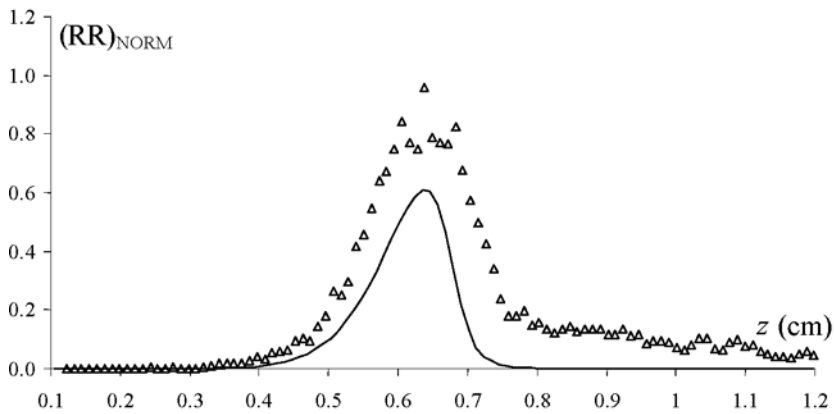
Figure 10. Experimental (triangles) and computational (solid line) normalized CO LIF signals, OH LIF signals, and RR along a line parallel to the axis of symmetry at a radial distance of 1 cm. The oxidizer nozzle is at $z = 0.0$ cm and the fuel nozzle is at $z = 1.3$ cm.



(a)



(b)



(c)

Figure 11. Experimental (triangles) and computational (solid line) normalized CO LIF signals, OH LIF signals and RR along a line parallel to the axis of symmetry at a radial distance of 2 cm. The oxidizer nozzle is at $z = 0.0$ cm and the fuel nozzle is at $z = 1.3$ cm.

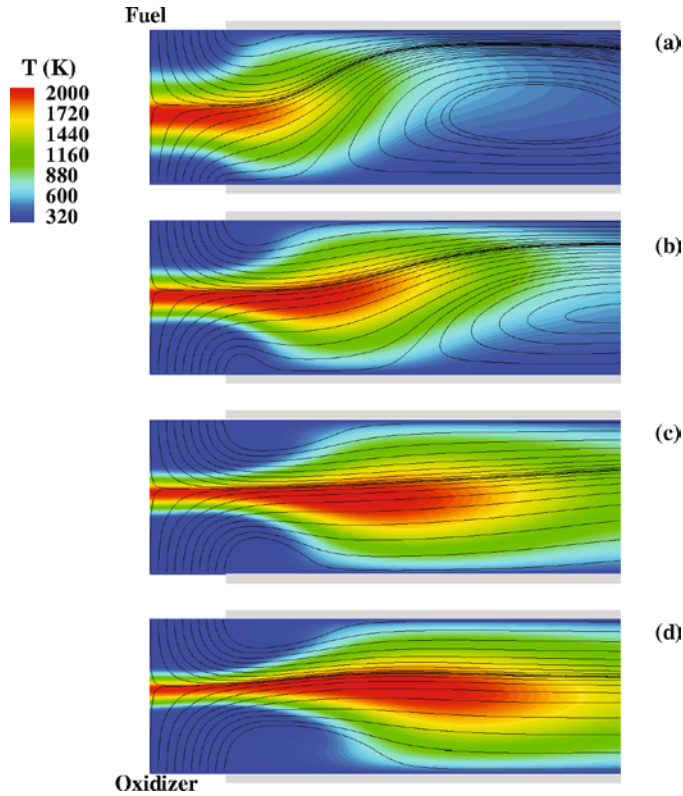


Figure 12. Streamlines superimposed on temperature maps for four flames at strain rates (a) 26 s^{-1} , (b) 77 s^{-1} , (c) 130 s^{-1} , and (d) 179 s^{-1} . The radial and axial extent of the computational images is $r = 4 \text{ cm}$ and $z = 1.3 \text{ cm}$, respectively. Streamlines are not shown at equispaced values of stream function.

result, the kinematic viscosity of the mixture near the edge of the oxidizer nozzle is increased, and, accordingly, the local Reynolds number is decreased. Hence, at low strain rates the flow on the oxidizer side is less likely to separate as compared with the fuel side. As the strain rate is increased, the flame thickness decreases and the thermal layer recedes away from the bottom nozzle. Consequently, the kinematic viscosity near the edge of the bottom nozzle becomes comparable to that at the top nozzle. This lower kinematic viscosity coupled with the higher inertia of the two opposing jets makes the separation of the ensuing recirculation zones inevitable on both sides.

Buoyancy plays a role in determining the growth of the two recirculation regions. At the low strain rate, the thermal layer is shifted toward the upper flange, preventing the upper recirculation region from growing, but allowing the lower recirculation zone to grow freely. In addition, figures 12(a) and 12(b) illustrate the existence of a separation region that recirculates gases from the outer boundary into the domain. The presence of this additional recirculation region requires a careful management of the computational boundary conditions at the outlet. The results for the lower strain rates in the outer region for figures 12(a) and 12(b) are probably only qualitative in nature, because Neumann boundary conditions were adopted throughout the simulations for lack of detailed experimental measurements at the outflow boundary. The presence of this recirculation region can be roughly estimated by equating the buoyant velocity and the radial velocity outside the nozzle region. The buoyant velocity can be approximated as $\sqrt{2gR \cdot \Delta\rho/\rho}$, where $\Delta\rho = \rho_{\text{COLD}} - \rho_{\text{HOT}}$, and the radial velocity outside the nozzle region

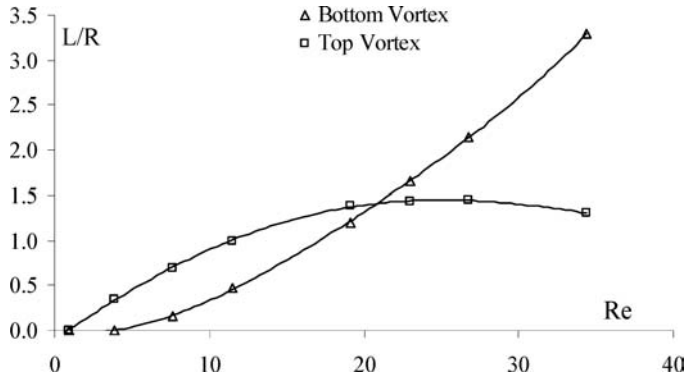


Figure 13. Evolution of the top and bottom recirculation lengths, normalized with respect to nozzle radius, as functions of Reynolds number. Recirculation length is computed as described in the text.

can be approximated as $AR \cdot R/r$. This velocity balance yields an estimate for the radial distance r at which separation occurs. A Richardson number based on the ratio of the square of these two velocities can be constructed showing the relative importance of the buoyancy in the z -direction over the radial momentum. This quantity scales as

$$Ri = \frac{2gR\Delta\rho}{\rho} \cdot \frac{r^2}{A^2R^4} \approx \frac{r^2}{A^2} \quad (12)$$

As a result, at a fixed radial coordinate, buoyancy will have a decreasing role as the strain rate is increased, whereas at a fixed strain rate the role of buoyancy will become increasingly significant farther away from the centreline. These observations are entirely consistent with our computational findings in figure 12.

Figure 13 illustrates the evolution of the radial dimension L of the recirculation regions anchored at the top and bottom nozzle walls, normalized with respect to the burner radius, as a function of the Reynolds number (we considered the kinematic viscosity for the methane side) for flames with the same composition as flame 1 in table 1. The top recirculation region appears at a Reynolds number, Re , of 0.95, corresponding to a strain rate of 6.4 s^{-1} , while the bottom vortex is not established until $Re = 3.8$, corresponding to a strain rate of 25.5 s^{-1} . The size of the bottom vortex initially increases with increasing Reynolds number, eventually reaching a peak value, and ultimately decreases with further increase in strain. Throughout the explored range of Reynolds number, the size of the bottom vortex increases monotonically with the strain rate.

We next consider whether gravity influences the profiles in the vicinity of the centreline. Accordingly, we compute a Richardson number based on natural and forced convection, in the z -direction, which is given by

$$Ri_z = \frac{2gR\Delta\rho}{\rho} \cdot \frac{1}{V_0^2} = \frac{2gR\Delta\rho}{\rho} \cdot \frac{1}{A^2R^2} = \frac{2g\Delta\rho}{\rho A^2R} \quad (13)$$

as a function of the strain. A comparison of our computational results with or without gravity shows that gravity plays a role in determining the centreline position of the flame only at strain rates of 6.4 s^{-1} or less, corresponding to $Ri_z \geq 15.6$.

In summary, the flow field of these 2D flames can be roughly partitioned into two regions: the counterflow region between the two reactant nozzles, and a radial development region which is initially confined by the two recirculation zones and, depending on the relevant Richardson numbers, may develop into a Poiseuille-type of flow. Buoyancy is virtually irrelevant in the first region at all but the smallest strain rates. Buoyancy, on the other hand, does play a role in

the growth of the recirculation zones and may ultimately result in recirculation at the outer flow boundary, which would dramatically complicate the definition of the appropriate boundary conditions.

In figure 14, the mass fraction of CH_4 , O_2 , H_2O , CO_2 , N_2 and the mixture fraction Z are reported for the flame illustrated in figures 6 to 11 and 12(c), whose strain rate is 130 s^{-1} . The mixture fraction is based on the linear combination of C, H and O mass fractions as defined by Bilger [24]. Figures 14(a)–(e) show that the recirculations at the exit of the nozzles convect reactants and products from the outer periphery back to the inlets of the burner. As combustion occurs, reactants are burnt, and their concentration decays in the radial direction. A small

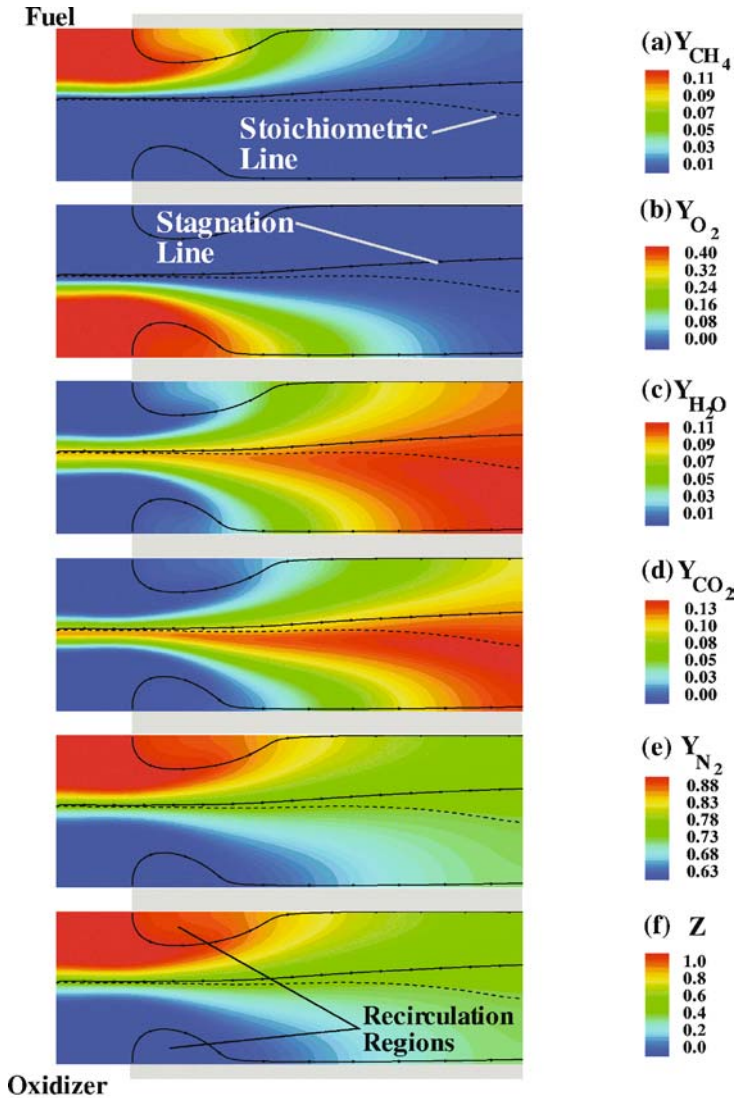


Figure 14. Major species isopleths: (a) methane mass fraction, (b) molecular oxygen mass fraction, (c) water vapour mass fraction, (d) carbon dioxide mass fraction, and (e) nitrogen mass fraction, (f) mixture fraction. The dividing streamlines of the recirculation regions and the stagnation surface are shown as solid lines, and the stoichiometric surface is represented by the dashed line.

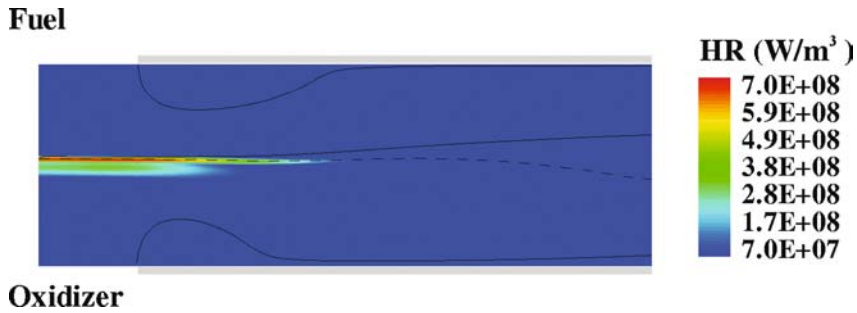


Figure 15. 2D image of the heat release rate. Recirculation regions, stagnation surface, and stoichiometric surface are also shown, similar to figure 14.

leakage of methane and oxygen through the far radial outlet of the domain is observed. The peak mass fractions of H_2O and CO_2 occur in different locations in the outer periphery of the domain. Furthermore, the images of mixture fraction [figure 14(f)] and nitrogen [figure 14(e)] are virtually identical.

The heat release layer in figure 15 tracks the reactive-diffusive boundary layer and consists of two zones, both located on the oxidizer side of the stagnation plane. The heat release rate HR can be expressed as

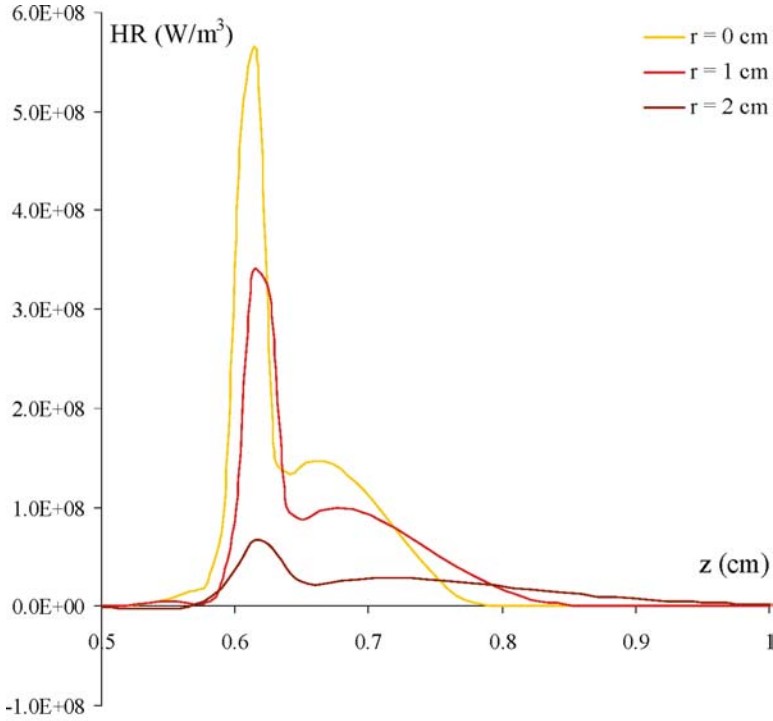
$$\text{HR} = \sum_{k=1}^{\text{NSPEC}} h_k \dot{\omega}_k W_k, \quad (14)$$

where W_k and h_k are the molecular weight and the enthalpy of formation for species k , respectively, and the quantity $\dot{\omega}_k$ represents the production rate of the k th species.

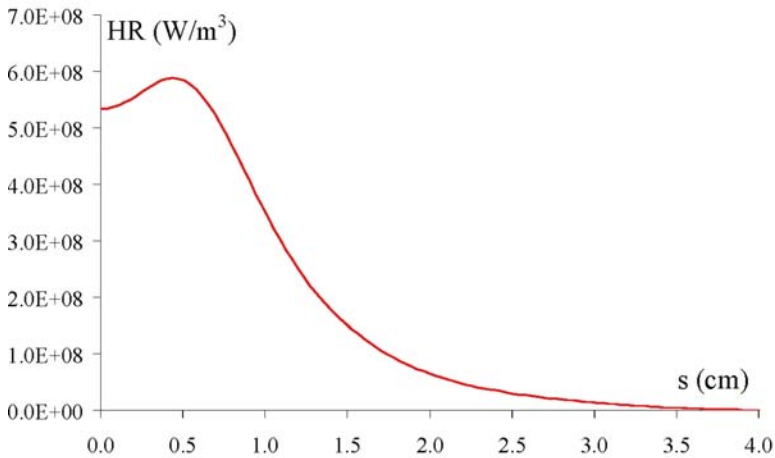
In figure 15, the first zone of heat release is a narrow region and is located closer to the stagnation plane, whereas the second zone is a wider, more diffuse region with a much lower heat release peak. The existence of this secondary peak was first reported in 1D calculations of counterflow flames in [25]. We will refer to these zones as the primary and the secondary heat release regions, respectively. Our computational results indicate that the relative integrated (along the axis of symmetry) contribution of these two zones to the total heat release rate amounts to 51% for the primary region and 49% for the secondary region.

Figure 16(a) presents 1D profiles of heat release rate along the lines $r = 0$ cm, $r = 1$ cm, $r = 2$ cm. These axial profiles show that the heat release layer is thinner in the nozzle region and thickens in the region between the flanges, where the scalar dissipation is lower. Furthermore, these axial scans illustrate the two peaks (primary and secondary) previously analysed in figure 15. Figure 16(b) presents 1D cuts along the stoichiometric surface. This surface is the location where the ratio between Y_{CH_4} and Y_{O_2} equals the stoichiometric ratio. The heat release rate increases locally near the axis of symmetry, owing to an increase in scalar dissipation rate, caused by the non-uniform velocity profile at the nozzle inlets, and eventually decreases, as the scalar dissipation decreases.

Tables 2 and 3 analyse the reactions that contribute to the primary and the secondary heat release regions, respectively. From table 2, we notice that the primary contributors to the sharp and narrow heat release peak are key oxidation steps for CH_3 , CH_2O , CH and H_2 , whereas the data in table 3 show that the secondary, more diffuse, region involves predominantly H radical recombination chemistry. This result is not mentioned in [25], possibly because the reaction $\text{OH} + \text{CO} \rightarrow \text{H} + \text{CO}_2$ is considered part of the secondary peak. This reaction occurs between the two maxima of heat release, closer to the primary peak. In addition, reference [25] considers forwards and backwards RRs separately. When the net contribution is considered, these two production rates can cancel each other out. For the flames considered



(a)



(b)

Figure 16. (a) 1D cuts for heat release rate in the axial direction at radial locations $r = 0$ cm, $r = 1$ cm, $r = 2$ cm. (b) Heat release rate as a function of curvilinear distance along the stoichiometric contour.

here, the reaction $\text{H} + \text{O}_2 = \text{O} + \text{OH}$ is at equilibrium, since the forward and backward production rates cancel each other.

Figure 17 reports a 2D image of scalar dissipation rate χ and the corresponding 1D cut along the stoichiometric surface. The highest values of the scalar dissipation rate are obtained in the region between the nozzles, and the maximum value is reached away from the axis of

Table 2. Chemical reactions that contribute to the peak of the primary heat release.

Reaction	Max % local heat release	A	β	E_a
$O + CH_3 = H + CH_2O$	21	$8.430E + 13$	0.000	0.00
$CH + H_2O = H + CH_2O$	17	$1.713E + 13$	0.000	-755.00
$OH + H_2 = H + H_2O$	15	$2.160E + 08$	1.510	3430.00
$H + O_2 = O + OH$	-14	$8.300E + 13$	0.000	14413.00
$OH + CH_2O = HCO + H_2O$	11	$3.430E + 09$	1.180	-447.00
$OH + CO = H + CO_2$	9	$4.760E + 07$	1.228	70.00
$HCO + H_2O = H + CO + H_2O$	-10	$2.244E + 18$	-1.000	17000.00
$H + C_2H_2 = C_2H_3$	-7	$0.224E + 34$	-6.697	8162.12
$H + CH_2O = HCO + H_2$	7	$2.300E + 10$	1.050	3275.00
$H + CH_3 = CH_4$	7	$0.204E + 32$	-5.685	4323.77

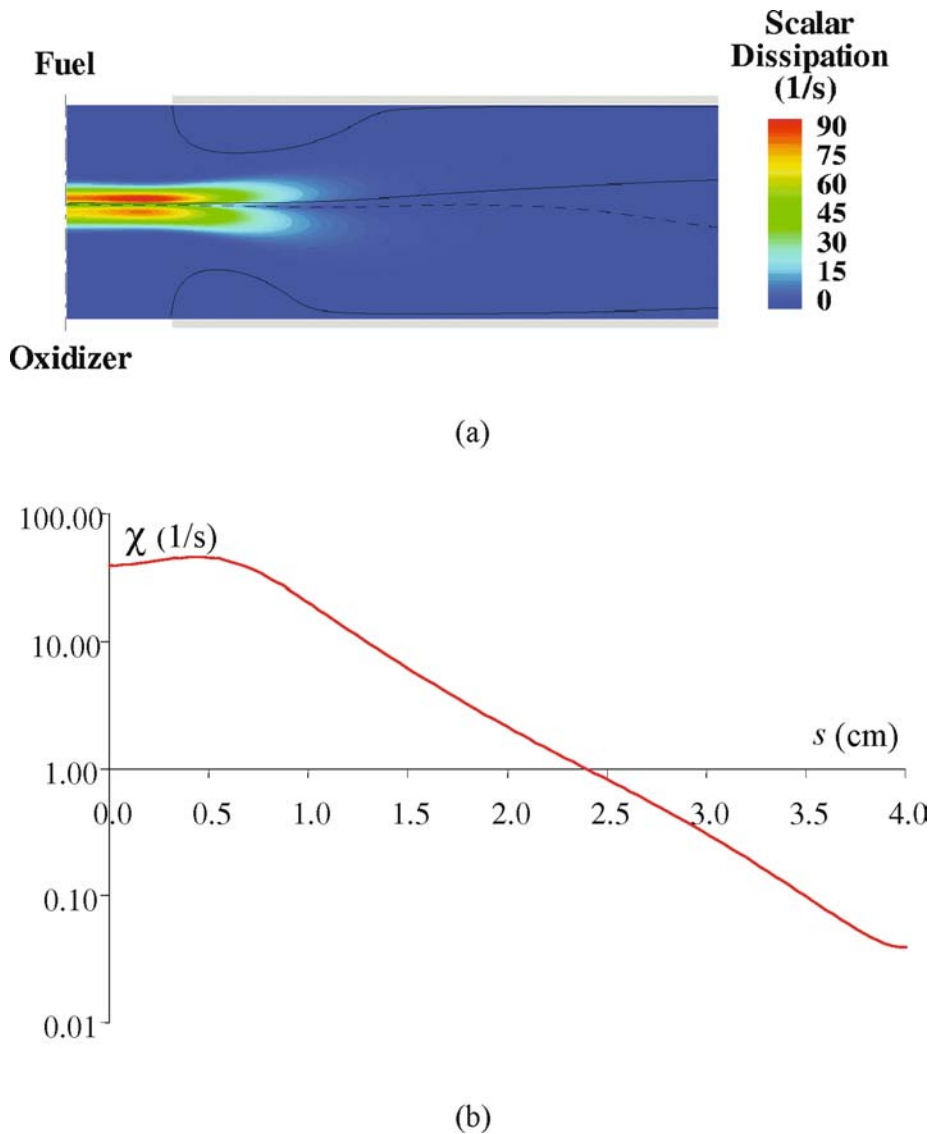


Figure 17. (a) 2D image of the scalar dissipation rate. The radial and axial extent of the computational domain are $r = 4.0$ cm and $z = 1.3$ cm, respectively. (b) Scalar dissipation rate as a function of curvilinear distance s along the stoichiometric surface. Recirculation regions, stagnation surface, and stoichiometric surface are also shown, similar to figure 14.

symmetry as a result of the non-uniform inlet velocity profile. On a semi-logarithmic scale, the graph in figure 17(b) reports the decay of the scalar dissipation rate as a function of the curvilinear distance, s , along the stoichiometric surface. This figure shows that, as the flow moves out of the nozzle region, the mixture fraction gradient at the stoichiometric surface decreases, which indicates that the mixing layer is growing. Interestingly, this decay along the stoichiometric surface is exponential. This result is possibly connected to the bounded nature of this counterflow geometry.

Figure 18 presents a 2D image for the temperature field and a cut along the stoichiometric surface. Along this surface, the temperature is lower in the vicinity of the axis of symmetry owing to the high scalar dissipation rate, and it decays close to the outlet of the domain owing to the heat transfer to the water-cooled flanges. The temperature peaks at $r = 1.636$ cm, well away from the region between the nozzles.

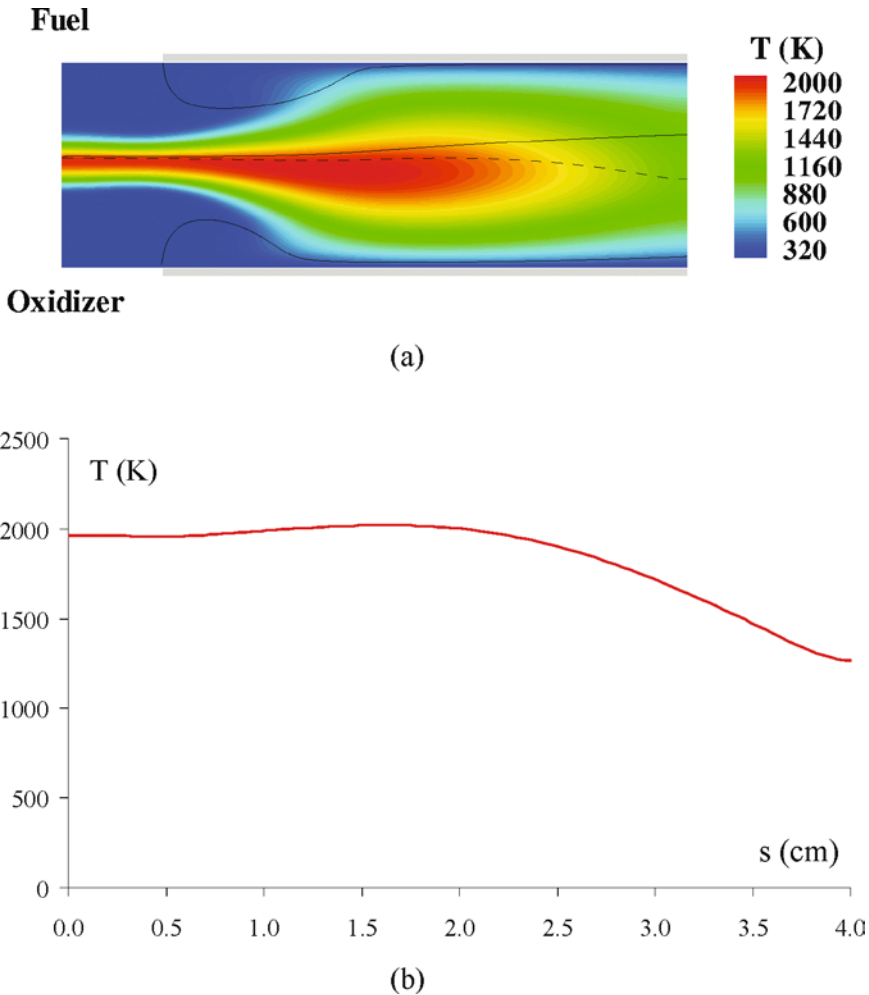


Figure 18. (a) 2D image of the temperature field. The radial and axial extent of the computational domain are $r = 4.0$ cm and $z = 1.3$ cm, respectively. (b) Temperature as a function of curvilinear distance s along the stoichiometric surface. Recirculation regions, stagnation surface, and stoichiometric surface are also shown, similar to figure 14.

Table 3. Chemical reactions that contribute to the peak of the secondary heat release.

Reaction	Max % local heat release	A	β	E_a
$\text{H} + \text{O}_2 + \text{H}_2\text{O} = \text{HO}_2 + \text{H}_2\text{O}$	27	9.380E + 18	-0.760	0.00
$\text{H} + \text{OH} + \text{M} = \text{H}_2\text{O} + \text{M}$	17	2.200E + 22	2.000	0.00
$\text{H} + \text{HO}_2 = 2\text{OH}$	10	1.340E + 14	0.000	635.00
$\text{OH} + \text{HO}_2 = \text{O}_2 + \text{H}_2\text{O}$	10	2.900E + 13	0.000	-500.00
$\text{O} + \text{HO}_2 = \text{OH} + \text{O}_2$	6	2.000E + 13	0.000	0.00
$\text{H} + \text{O}_2 + \text{N}_2 = \text{OH} + \text{O}_2 + \text{N}_2$	4	3.750E + 20	-1.720	0.00
$\text{H} + \text{O}_2 + \text{M} = \text{HO}_2 + \text{M}$	3	2.800E + 18	-0.860	0.00
$\text{OH} + \text{OH} = \text{H}_2\text{O}_2$	3	1.280E + 18	-2.420	-551.96
$\text{H} + \text{HO}_2 = \text{H}_2 + \text{O}_2$	3	2.800E + 13	0.000	1068.00
$\text{OH} + \text{H}_2\text{O}_2 = \text{H}_2\text{O} + \text{HO}_2$	1	2.720E - 02	4.550	-3203.00

5. Conclusions

A 2D computational study of the structure of a steady, axisymmetric, methane/enriched-air, laminar opposed-jet diffusion flame, was quantitatively validated with respect to measurements of the velocity field, CO LIF, OH LIF, and the forward reaction rate of the reaction $\text{CO} + \text{OH} \rightarrow \text{CO}_2 + \text{H}$. Computationally, we solved the steady state equations in a modified vorticity-velocity formulation, in which the Poisson-like equation for the radial velocity was replaced by the continuity equation. The comparison between the experimental and computational data yielded excellent agreement for all the measured quantities.

The careful design of a burner with well-defined boundary conditions was critical for achieving this level of agreement. In particular, it was found that practical counterflow configurations inevitably present non-uniformities in the radial distribution of the inlet axial velocity, preventing the imposition of simple boundary conditions from the measurements of global quantities, such as the mass averaged inlet axial velocity.

The flow field of these 2D flames can be approximately partitioned into two regions: the counterflow region between the two reactant nozzles, in which viscous and diffusive effects are confined to the mixing layer and to the nozzle walls where separation occurs, and a radial development region which is initially confined by the recirculation zones and, depending on strain rates and relevant Richardson numbers, may ultimately develop into a Poiseuille-type of flow. Buoyancy is insignificant in the first region at all but the smallest strain rates. Buoyancy does play a role in the growth of the recirculation zones and in determining the flame location in the outermost region. At low strain rates a buoyancy-induced recirculation zone may stabilize at the domain outlet, complicating the specification of the outlet boundary conditions.

Acknowledgements

This research was supported by NSF, Grant No. CTS-9904296 (Dr Farley Fisher, Contract Monitor) and the US Department of Energy, Office of Basic Energy Sciences, Division of Chemical Sciences, Geosciences, and Biosciences. The technical assistance of N. Bernardo (Yale University) and R. Sigurdsson, (Sandia National Laboratories), in the construction of the hardware and in setting-up the optical diagnostic system, respectively, and technical discussions with Professor A. Linan, Dr Beth Anne Bennett and Dr James A. Cooke are gratefully acknowledged. The authors thank Drs T. C. Williams and R. W. Schefer for the use of the PIV facility at Sandia National Laboratories.

References

- [1] Katta, V.R., Carter, C.D., Fiechtner, G.J., Roquermore, W.M., Gord, J.R. and Rolon, J.C., 1998, Interaction of a vortex with a flat flame formed between opposing jets of hydrogen and Air. *Proceedings of the Combustion Institute*, **27**, 587–594.
- [2] Oh, C.B., Lee, C.E. and Park, J., 2004, Numerical investigation of extinction in a counterflow nonpremixed flame perturbed by a vortex. *Combustion and Flame*, **138**, 225–241.
- [3] Frouzakis, C.E., Lee, J., Tomboulides, A.G. and Boulouchos, K., 1998, Two-dimensional direct numerical simulation of opposed-jet hydrogen-air diffusion flame. *Proceedings of the Combustion Institute*, **27**, 571–577.
- [4] Lee, J., Frouzakis, C.E. and Boulouchos, K., 2000, Two-dimensional numerical simulation of opposed-jet hydrogen/air flames/transition from a diffusion to an edge flame. *Proceedings of the Combustion Institute*, **28**, 801–806.
- [5] Frouzakis, C.E., Tomboulides, A.G., Lee, J. and Boulouchos, K., 2002, Transient phenomena during diffusion/edge transitions in an opposite jet hydrogen/air burner. *Proceedings of the Combustion Institute*, **29**, 1581–1587.
- [6] Katta, V.R., Meyer, T.R., Brown, M.S., Gord, J.R. and Roquermore, W.M., 2004, Extinction criterion for unsteady, opposing-jet diffusion flames. *Combustion and Flame*, **137**, 198–221.
- [7] Katta, V.R., Hsu, K.Y. and Roquermore, W. M., 1998, Local extinction in an unsteady methane-air jet diffusion flame. *Proceedings of the Combustion Institute*, **27**, 1121–1129.
- [8] Ern, A. and Smooke, M.D., 1993, Vorticity–velocity formulation for three-dimensional steady compressible flows. *Journal of Computational Physics*, **105**, 58–71.
- [9] Frank, J.H., Kaiser, S.A. and Long, M.B., 2002, Reaction-rate, mixture fraction, and temperature imaging in turbulent methane/air jet flames. *Proceedings of the Combustion Institute*, **29**, 2687–2694.
- [10] Rehm, J.E. and Paul, P.H., 2000, Reaction rate imaging. *Proceedings of the Combustion Institute*, **28**, 1775–1782.
- [11] Gomez, A. and Rosner, D.E., 1993, Thermophoretic effects on particles in counterflow laminar diffusion flames. *Combustion Science and Technology*, **89**, 335–362.
- [12] Wolfram, S., 1996, *The Mathematica Book*, third edition (Cambridge: Wolfram Media/Cambridge University Press).
- [13] Smooke, M.D., Xu, Y., Zurn, R.M., Lin, P., Frank, J.H. and Long, M.B., 1992, *Proceedings of the Combustion Institute*, **24**, 813–821.
- [14] Hall, R.J., 1995, The radioactive source term for plane-parallel layers of reacting combustion gases. *Journal of Quantitative Spectroscopy and Radiative Transfer*, **49**, 517–523.
- [15] Smooke, M.D., Mitchell, R.E. and Keyes, D.E., 1989, Numerical solution of 2-dimensional axisymmetric laminar diffusion flames. *Combustion Science and Technology*, **67**, 85–122.
- [16] Chelliah, H.K., Law, C.K., Ueda, T. and Smooke, M.D., 1990, An experimental and theoretical investigation of the dilution, pressure and flow-field effects on the extinction condition of methane–air–nitrogen diffusion flames. *Proceedings of the Combustion Institute*, **23**, 503–511.
- [17] Settersten, T.B., Dreizler, A. and Farrow, R.L., 2002, Temperature- and species-dependent quenching of CO B $^1\Sigma^+(v=0)$ probed by two-photon laser-induced fluorescence using a picosecond laser. *Journal of Chemical Physics*, **117**, 3173–3179.
- [18] Tamura, M., Berg, P.A., Harrington, J.E., Luque, J., Jeffries, J.B., Smith, G.P. and Crosley, D.R., 1998, Collisional quenching of CH(A), OH(A), and NO(A) in low pressure hydrocarbon flames. *Combustion and Flame*, **114**, 502–514.
- [19] Luque, J. and Crosley, D.R., 1998, Transition probabilities in the A $^2\Sigma^+ - X^2\Pi$ electronic system of OH. *Journal of Chemical Physics*, **109**, 439–448.
- [20] Di Rosa, M.D. and R.L. Farrow, R.L., 1999, Two-photon excitation cross section of the B \leq X(0, 0) band of CO measured by direct absorption. *Journal of the Optical Society of America B*, **16**, 1988–1994.
- [21] Kaiser, S.A., Frank, J.H. and Long, M.B., 2005, Use of Rayleigh imaging and ray tracing to correct for beam-steering effects in turbulent flames. *Applied Optics*, **44**, 6657–6654.
- [22] Gardiner, W.C. Jr., Hidaka, Y. and Tanzawa, T., 1981, Refractivity of combustion gases. *Combustion and Flame*, **40**, 213–219.
- [23] Seshadri, K. and Williams, F.A., 1978, Laminar-flow between parallel plates with injection of a reactant at high Reynolds-number. *International Journal of Heat Mass Transfer*, **21**, 251–253.
- [24] Bilger, R.W., 1988, The structure of turbulent nonpremixed flames. *Proceedings of the Combustion Institute*, **22**, 475–488.
- [25] Sung, C.J., Liu, J.B. and Law, C.K., 1995, Structural response of counterflow diffusion flames to strain rate variations. *Combustion and Flame*, **102**, 481–492.